

Nanoscale

Accepted Manuscript



This is an *Accepted Manuscript*, which has been through the Royal Society of Chemistry peer review process and has been accepted for publication.

Accepted Manuscripts are published online shortly after acceptance, before technical editing, formatting and proof reading. Using this free service, authors can make their results available to the community, in citable form, before we publish the edited article. We will replace this *Accepted Manuscript* with the edited and formatted *Advance Article* as soon as it is available.

You can find more information about *Accepted Manuscripts* in the [Information for Authors](#).

Please note that technical editing may introduce minor changes to the text and/or graphics, which may alter content. The journal's standard [Terms & Conditions](#) and the [Ethical guidelines](#) still apply. In no event shall the Royal Society of Chemistry be held responsible for any errors or omissions in this *Accepted Manuscript* or any consequences arising from the use of any information it contains.

ARTICLE

Cite this: DOI: 10.1039/x0xx00000x

Micro-nano structured Ni-MOFs as high-performance cathode catalyst of rechargeable Li–O₂ batteriesXiaofei Hu¹, Zhiqiang Zhu¹, Fangyi Cheng¹, Zhanliang Tao¹ and Jun Chen^{1,2*}Received 00th January 2012,
Accepted 00th January 2012

DOI: 10.1039/x0xx00000x

www.rsc.org/

Rechargeable Li–O₂ batteries with high theoretical energy density urgently require efficient cathode catalysts to improve their electrochemical performance. Here we first demonstrated the application of Ni-based-organic frameworks of Ni(4,4'-bipy)(H₃BTC) (4,4'-bipy = 4,4'-bipyridine; H₃BTC = 1,3,5-benzenetricarboxylic acid) (Ni-MOFs) as high-performance cathode catalyst of rechargeable Li–O₂ batteries. It is found that Ni-MOFs with three-dimensional (3D) micro-nano structure, open catalytic sites and large specific surface area have guaranteed the free transfer of O₂ and effective contact between the electrolyte and the catalytic sites. A preliminary test of Ni-MOFs showed an extremely high capacity of 9000 mAh g⁻¹, a high round-trip efficiency of 80%, and a respectable cycling of 170 cycles without obvious voltage drop. Furthermore, plastic rechargeable Li–O₂ batteries with Ni-MOFs as the cathode catalyst have been assembled, displaying an energy density of 478 Wh kg⁻¹. This study leads to both fundamental and technological advances of Ni-MOFs as the cathode of rechargeable Li–O₂ batteries.

Introduction

Metal-organic frameworks (MOFs), which are made by linking metal ions/clusters and organic ligands through coordination bonds, represent an emerging class of porous crystalline compounds.^{1–4} Porous MOFs have shown attractive interest in the fields such as gas separation and hydrogen storage due to their uniform and permeable channels that can not only provide countless active sites on the pore surface but also facilitate the diffusion of gas and/or ions.^{5–10} Recent study has shown that Ni nanoparticles supported on carbon, which were prepared with the decomposition of Ni-based MOFs of Ni(4,4'-bipy)(H₃BTC) (4,4'-bipy = 4,4'-bipyridine; H₃BTC = 1,3,5-benzenetricarboxylic acid) (here denoted as Ni-MOFs), can be used as efficient catalysts for hydrolysis of ammonia borane.¹¹ Thus, how to further develop the application of Ni-MOFs is of great importance.

Rechargeable metal-air batteries such as lithium–oxygen (Li–O₂) batteries with oxygen reduction/evolution reactions (ORR/OER) on the cathode have recently attracted extensive attention due to their high theoretical energy density (3155 Wh kg⁻¹, based on the mass of discharge product Li₂O₂).^{12–17} However, the sluggish ORR/OER in the cathode of Li–O₂ batteries results in large overpotential (i.e. low round-trip efficiency), poor cycling life and low rate capability. This seriously limits the battery performance.^{18–20} Thus, much effort has been devoted to exploiting cathode catalysts to promote ORR/OER. Porous gold has demonstrated the great promotion of ORR/OER due to the accommodation of insoluble Li₂O₂ that

is generated during the discharge.²¹ Mn-MOFs with one-dimensional channels as cathode catalysts in nonaqueous Li–O₂ batteries exhibited 30 cycles with fixed capacity of 1000 mAh g⁻¹ at 250 mA g⁻¹.²² Generally, the cathode catalysts with high surface areas and abundant catalytic sites are preferred because they can enhance the effective contact between the electrolyte and catalysts.

We here report, for the first time, the use of Ni-MOFs as a promising cathode catalyst for room-temperature rechargeable nonaqueous Li–O₂ batteries. Ni-MOFs possess two sorts of uniform 3D tricontinuous microchannels (5–8 Å and 6–7 Å as the channel sizes) and nanopores (500 Å) with a high Brunauer-Emmett-Teller (BET) surface area of 1225 m² g⁻¹, which guarantees the controlled transfer of O₂ and Li⁺ as well as the sufficient contact between the electrolyte and catalytic metal sites. As the cathode catalyst of Li–O₂ batteries, Ni-MOFs significantly promote the ORR/OER. An extremely high discharge capacity of 9000 mAh g⁻¹ at 0.12 mA cm⁻² was obtained. Meanwhile, a high round-trip efficiency of 80% and a long cycling of 170 cycles were obtained with a cut-off capacity of 600 mAh g⁻¹ at 0.6 mA cm⁻². Furthermore, a plastic Li–O₂ cell with the energy density of 478 Wh kg⁻¹ was successfully fabricated. This study demonstrates the application extension of Ni-MOFs-based cathode in Li–O₂ batteries with reversible electrochemical ORR/OER.

Experimental section**Synthesis Procedures**

All reagents are of analytical grade and used as received. Ni(4,4'-bipy)(HBTC) (4,4'-bipy = 4,4'-bipyridine; H₃BTC = 1,3,5-benzenetricarboxylic acid) (Ni metal-organic framework, Ni-MOFs) was solvothermally prepared with the modification of previous report.²³ 4,4'-bipy of 0.576 g (3 mmol), H₃BTC of 0.633 g (3 mmol), and Ni(NO₃)₂·6H₂O of 0.876 g (3 mmol) were dissolved in N,N-dimethylformamide (DMF) of 60 mL and stirred vigorously for 5 min at room temperature. Then, the obtained green solution was sealed in a teflon-lined autoclave with the volume of 100 mL and kept at 80 °C with dwell time of 70 h. After cooling to room temperature in ambient air, the autoclave was opened. The green crystal-like solid was collected by centrifuging at 9500 rpm and washing thoroughly with DMF three times. Finally, the obtained green crystals were dried at 180 °C for 6 h under vacuum.

Material Characterization

Ni-MOFs, C, and discharge products were characterized by powder X-ray diffraction (XRD, Rigaku MiniFlex600, Cu K α) radiation and Raman microscope (DXR, Thermo-Fisher Scientific, 532 nm excitation). The Brunauer-Emmett-Teller (BET) specific surface area was detected by the N₂ adsorption-desorption isotherm at 77 K (BELSORP-mini instrument). The morphology and element distribution of Ni-MOFs, C, and discharge products were observed by field-emission scanning electron microscopy (SEM, JEOL JSM7500F). The microstructures of Ni-MOFs were measured by transmission electron microscopy (TEM, Tecnai G2 F20) under 200 kV in vacuum.

Electrochemical Test

Ni-MOFs electrodes were fabricated by casting a mixture of 30 wt% Ni-MOFs, 60 wt% Vulcan carbon XC-72, 10 wt% polyvinylidene fluoride (PVDF) on a pressed nickel foam current collector. For C electrodes, no Ni-MOFs was used and the weight ratio of Vulcan carbon XC-72 and PTFE was 9:1. The total mass loading of the two electrodes are ~ 0.5 mg cm⁻² (the mass of each piece of Ni foam is about 15 mg). Electrochemical studies were conducted using CR2032 coin-type cells, employing Ni-MOFs or C electrode as cathode catalyst with a lithium foil as anode and a glass fiber (16 mm in diameter, 0.3 mm in thickness, porosity of 92%–98%) as separator. The electrolyte is 1 M lithium bis-(trifluoromethanesulfonyl)-imide (LiTFSI) in tetraethylene glycol dimethyl ether (TEGDME).

Plastic Li–O₂ batteries (PLOBs, soft package style) were also fabricated and investigated. For a PLOB, it was one plastic bag filled with a lithium foil anode (1.2×4 cm²), a glass fiber separator (1.4×4.2 cm², 0.3 mm in thickness, porosity of 92%–98%), and an air electrode (1.2×4 cm², 16 mg of Ni-MOFs coating on one piece of carbon paper) with a total mass of 360 mg. The cathode side of the plastic bag was dug many holes for O₂ transfer. The anode was fixed on the inner bottom of the plastic bag by double-side tape. The electrolyte was 1 M LiTFSI in TEGDME. Electroconductive paste was used to fix two conductive wires on lithium foil and carbon paper,

respectively. A clip was used to nip the plastic bag in order to fix all the electrodes and the separator. All procedures for the cell assembly were carried out in an argon-filled glove box (Mikrouna Universal 2440/750, moisture content and oxygen level < 1 ppm). The assembled CR2032 coin type batteries and PLOBs were set into a sealed glass bottle filled with pure oxygen at 1 atm at temperature. These batteries were tested by galvanostatic experiments on a LAND battery testing system at room temperature after 8 h rest period. Cyclic voltammograms (CVs) were recorded on Parstat 263A potentiostat/galvanostat workstation (Princeton Applied Research & AMETEK Company). Electrochemical impedance spectroscopy (EIS) was measured on an AC voltage of 5 mV amplitude in the frequency range from 100 kHz to 0.1 kHz.

Rotating-Disk-Electrode (RDE) measurements

This work employed RDE technique.²⁴ Briefly, the electrochemical characterizations were conducted in a three-electrode electrochemical sink using a Pt foil as the counter electrode, a KCl-saturated calomel electrode (SCE) as the reference electrode, and a working electrode of a sample-coated glass carbon (GC) electrode, which is fixed in a rotating ring-disk electrode (RRDE, Pt ring and GC disk, disk radius 2.80 mm). The electrolyte is 1 M LiTFSI in TEGDME (0 V Li ≈ -3.28 V vs. Hg/Hg₂Cl₂), which was saturated with high-purity O₂ (Air Product, purity 99.995%). The catalyst sample 1 is a mixture of Ni-MOFs and Cabot Vulcan XC-72 at a ratio of 3 mg / 6 mg. The catalyst sample 2 is pure C of 9 mg. The mixture was ultrasonically dispersed in 900 mL of 850:50 v/v isopropyl alcohol/neutralized Nafion solution (5 wt%, Sigma-Aldrich) mixed solvent for 20 min to form a homogeneous ink. Then, 7.0 μ L of the catalyst ink (containing 70 μ g of catalyst) was loaded onto the glassy carbon electrode and naturally dried under isopropyl alcohol atmosphere overnight. The catalyst loading was approximately 0.284 mg cm⁻². The disk electrode was potentially scanned at a rate of 5 mV s⁻¹ from 3.28 to 2.28 V versus Li⁺/Li under rotating speed of 1600 rpm (ORR) and from 4.18 to 3.28 V versus Li⁺/Li under rotating speed of 1600 rpm (OER). Before OER test, the RDE was conducted by holding the voltage at 2.48 V for 10 min.

Result

The morphology and structure of Ni-MOFs.

Fig. 1 shows the morphology, element distribution, and molecule structure of Ni-MOFs. As Fig. 1a displays, Ni-MOFs are in the form of blue powders with the shape of hexagonal plate (side length of ~ 5 μ m and thickness of ~ 1 μ m). Fig. 1b exhibits nanoporous structure in the side view of the hexagonal plates, revealing the uniform distribution of C, O, Ni, and N elements within Ni-MOFs. The powder XRD patterns of the as-synthesized Ni-MOFs were provided by Fig. S1a. The 2 θ values of the peaks of Ni-MOFs are in well agreement with the simulation,²³ demonstrating the success of the synthesis. We also observed Ni-MOFs by TEM. Since an ultrasonic method was used in the process of sample preparation, only

fragmentized samples could be observed (Fig. 1c). Interestingly, some dark dots (marked with circles) without any typical lattice fringes are found in the high resolution TEM (HRTEM) image (Fig. 1d). After the test for ~ 10 min, clearly lattice fringes emerged (inset of Fig. 1d). The measured distance between adjacent lattice fringes is approximately 0.21 nm, which is consistent with the spacing of (111) planes of nickel. This should be explained by the reduction of Ni^{2+} to Ni within original Ni-MOFs due to the electron beam irradiation. The molecule structure of Ni-MOFs is depicted in Fig. 1e. The framework of Ni-MOFs was assembled by two kinds of connecting ligands of H_3BTC and 4,4'-bipy as well as Ni^{2+} (triangular bipyramid type) centers. The honeycomb grid layers constructed by Ni^{2+} and H_3BTC are linked by 4,4'-bipy pillars to form a 3D tri-continuously porous framework. The red,

green, and blue rods stand for three cross linking channels, which are perpendicular to c-axis and equal to each other. In addition, the honeycomb like channels along c-axis (yellow rods) are $\sim 6 \text{ \AA} \times 7 \text{ \AA}$, while the pillars of 4,4'-bipy form rectangle channels that are $\sim 5 \text{ \AA} \times 8 \text{ \AA}$. The porous structure is confirmed by the N_2 adsorption-desorption analysis of the as-prepared Ni-MOFs, which shows a high BET surface area of $1225 \text{ m}^2 \text{ g}^{-1}$ (Fig. S1b) and a hysteresis loop (type IV, a signal of mesopores²⁵). Horvaih–Kawazoe (HK) pore size distribution at ~ 7 and $\sim 11 \text{ \AA}$ (the inset of Fig. S1b). The micro-channels and nanopores of Ni-MOFs are large enough for free transfer of O_2 (3.46 \AA) and electrolyte (containing Li^+). Such facts, along with the open metal sites that can enhance O_2 adsorption and catalysis,²⁶ should render Ni-MOFs a promising cathode catalyst for Li– O_2 batteries.

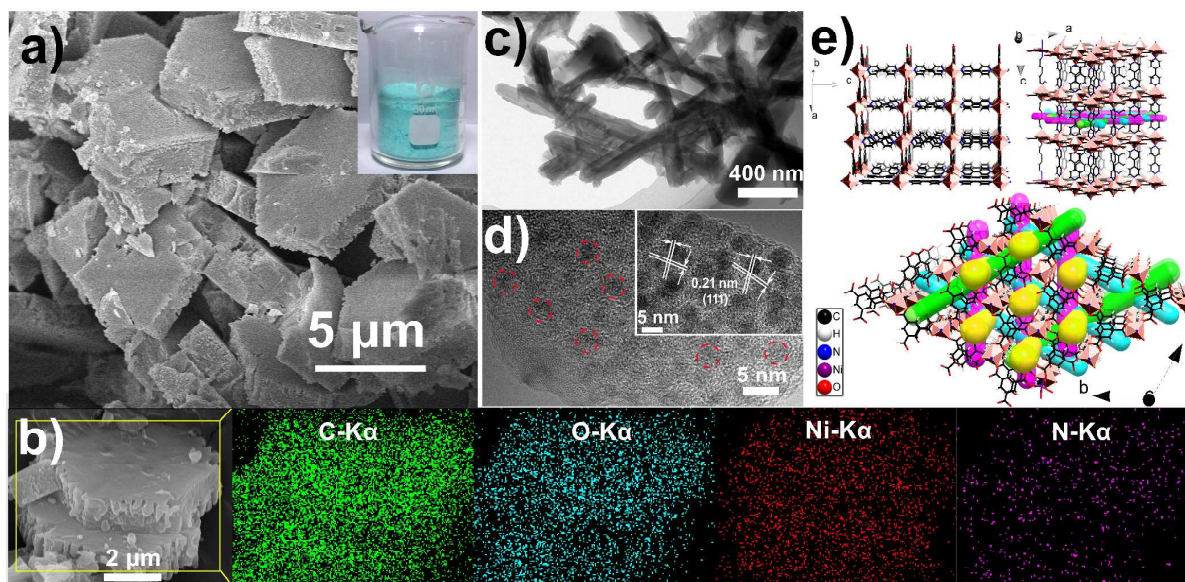


Fig. 1 The morphology and structure of Ni-MOFs. (a) SEM image of Ni-MOFs. The inset shows the optical photograph of Ni-MOFs in a glass beaker. (b) SEM image and carbon, oxygen, nickel, and nitrogen element mapping images of Ni-MOFs. The yellow box highlights the spectrum image. (c) TEM and (d) HRTEM image of Ni-MOFs under 200 kV in vacuum. The circles in (d) mark some of reduced Ni clusters. Inset of (d) presents the HRTEM image of Ni-MOFs after TEM test last ~ 10 min. (e) Crystal structures of Ni-MOFs along c axis, perpendicular to c axis and along b axis. The red, green, and blue rods stand for three cross linking channels, which are equal to each other. The yellow rods stand for channels along c axis.

Electrochemical performances on RDE.

To evaluate the catalytic performance of Ni-MOFs for Li– O_2 battery, we applied catalyst-loading rotation disk electrode (RDE) within electrolyte of 1 M LiTFSI in TEGDME (Fig. 2a). The electrode is composed of Ni-MOFs and conductive carbon (VC-72) (denoted as Ni-MOFs/C). For comparison, pure VC-72 has also been tested. Obviously, Ni-MOFs/C exhibit more positive ORR (2.84 V vs. Li^+/Li) and more negative OER (3.84 V vs. Li^+/Li) potential than those of VC-72, suggesting that Ni-MOFs/C are able to get smaller charge overpotential when used as cathode catalyst for Li– O_2 batteries.²⁵ This is further supported by the cyclic voltammety curves (obtained on RDE, Fig. 2b), in which Ni-MOFs/C own larger current density and smaller ORR/OER peak gap than that of perovskite-based porous $\text{La}_{0.75}\text{Sr}_{0.25}\text{MnO}_3$ nanotubes.²⁷ The improved catalytic

activity of Ni-MOFs is ascribed to the effective utilization of catalytic Ni atom (provided by the inner and outer surfaces of open nanoporous structure) and free transfer of O_2 in 3D continuous microchannels. The anodic process decomposed the discharge product, guaranteeing the reutilization of porous structure.

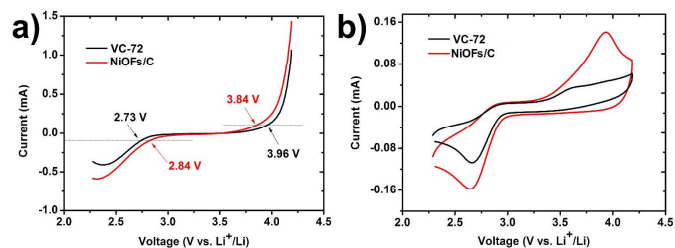


Fig. 2 (a) ORR and OER polarization curves of VC-72 and Ni-MOFs/C on rotating disk electrode (RDE) in O_2 -saturated aprotic electrolyte of 1 M LiTFSI in

TEGDME. (b) Cyclic voltammetry curves at 20 mV s^{-1} on RDE within O_2 -saturated 1 M LiTFSI in TEGDME.

Electrochemical performances in coin-type Li–O₂ batteries.

Ni-MOFs have been employed as cathode catalyst for Li–O₂ battery with a lithium foil as anode (Fig. 3a). The electrolyte is 1 M LiTFSI in TEGDME, which is one of the most stable electrolytes for Li–O₂ batteries known to date.²⁸ To increase the conductivity of the catalyst, the cathode was made by pasting the mixture of Ni-MOFs and Vulcan XC-72 (labeled as VC-72) onto a pressed Ni foam (details can be seen in Experimental Section). The outer side and inner side morphologies of the cathode are shown in Fig. S2a and b, respectively. Ni-MOFs based catalyst was only pasted on the inner side of Ni foam with smooth surface and few tiny cracks, so the outer side of the cathode is actually the pristine state of Ni foam with

macroporous structure that allow O₂ transport. The sectional views of the cathode (Fig. S2c) reveals that the Ni foam layer is not over compacted. In addition, Ni-MOFs own microporous structure ($6 \text{ \AA} \times 7 \text{ \AA}$ and $5 \text{ \AA} \times 8 \text{ \AA}$ channels). The cathode catalytic layer has abundant nanopores for accommodation of the discharge products (Fig. S2d). Consequently, Li⁺ and O₂ freely transfer to the interface between the electrolyte and the catalytic site of Ni²⁺ to form discharge products on discharging (ORR process), which will be decomposed on charging (OER process). The distribution of C, Ni, O, and N elements of the cathode is depicted in Fig. S2e, revealing that the bulk of Ni-MOFs was milled to small fragments and mixed uniformly with conductive carbon (VC-72). Furthermore, porous VC-72 offers large amount of temporary space for oxygen accommodation before discharge and after recharge.

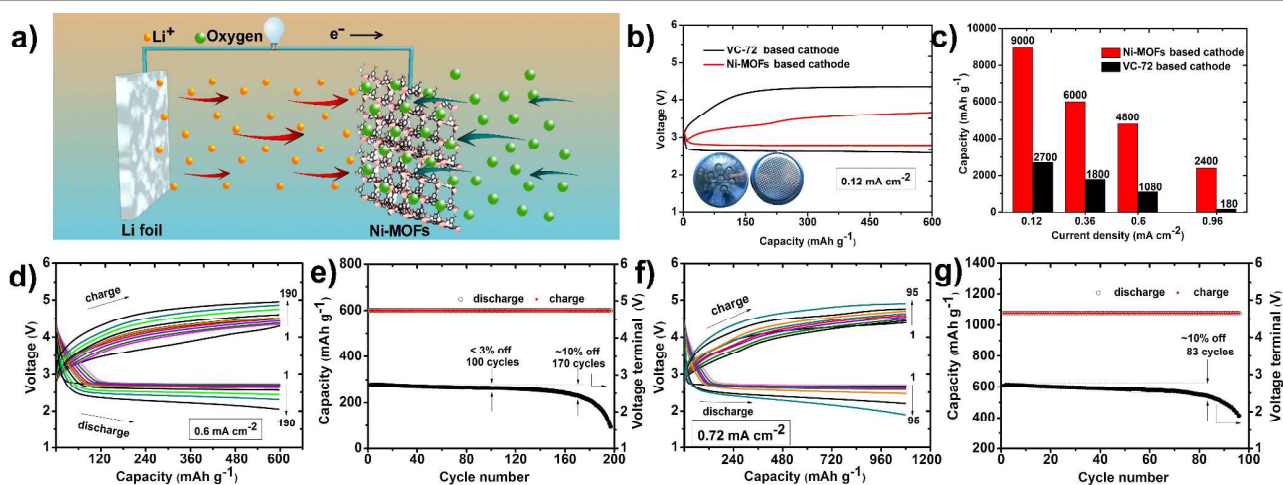


Fig. 3 Electrochemical performance of Ni-MOFs-based Li–O₂ batteries. (a) The scheme of a Li–O₂ battery: The battery mainly consists of a Li anode and an O₂ cathode within the electrolyte of 1 M LiTFSI in TEGDME. The cathode is a piece of Ni foam coated by Ni-MOFs. On discharging, the discharge product is produced by the reaction between Li⁺ (from organic electrolyte) and O₂, and finally deposited on the surface of cathode; while on charging, the deposited product gets decomposed to Li⁺ and O₂. (b) Typical voltage profiles of Ni-MOFs-based and VC-72 based Li–O₂ batteries with fixed capacity of 600 mAh g⁻¹ at 0.12 mA cm⁻². The inset shows the photographs of the CR2032 coin-type battery with positive and negative sides. (c) Comparison of discharge capacity of Ni-MOFs and VC-72 based cathodes at different current densities. (d, f) Galvanostatic discharge–charge curves and (e, g) variation of voltage on the discharge terminal of Li–O₂ batteries with fixed capacity of (d, e) 600 mAh g⁻¹ at 0.6 mA cm⁻² and (f, g) 1080 mAh g⁻¹ at 0.72 mA cm⁻². The capacity is based on the total mass loading on cathode including Ni-MOFs, VC-72, and binder. The current densities are based on current collector area.

The electrochemical performance of Ni-MOFs-based cathode was investigated using CR2032 coin-type Li–O₂ batteries (the inset of Fig. 3b) (see details in the Methods). A VC-72 based battery (without Ni-MOFs) has also been assembled for comparison. Unless specific stated, the capacity is calculated on the total mass of Ni-MOFs, VC-72, and binder on cathode; the current density is based on current collector area. Fig. 3b shows the discharge/charge profiles of the two cells with the capacity limit of 600 mAh g⁻¹, which is normally used for testing Li–O₂ batteries. The average discharge and charge voltage of Ni-MOFs-based cathode are 3.5 and 2.8 V, respectively, giving a super round-trip efficiency of 80%. It should also be stressed that the discharge overpotential of 0.16 V (the gap between the discharge voltage and the theoretical value of 2.96 V) is among the lowest values reported by far.^{29–33} In contrast, the overpotentials of C based cells in the discharging and charging are much higher. These results clearly confirm the high

ORR/OER activity of Ni-MOFs, which should be benefited from the permeable 3D channels and open metal sites.

Fig. 3c compares the discharge capacity of Ni-MOFs-based and VC-72-based cathodes at different current densities with voltage cut-off to 2.2 V. Clearly, Ni-MOFs-based cathode delivered much larger discharge capacity than that of C based cathode all the time, suggesting that Ni-MOFs can effectively enlarge the capacity of air cathode. Particularly, Ni-MOFs-based cathode realizes an extremely high capacity of 9000 mAh g⁻¹ at 0.12 mA cm⁻², which is 3.3 times higher than that of C based cathode. Furthermore, Ni-MOFs-based cathode also demonstrates superior fast charge/discharge ability, delivering a considerable discharge capacity of 2400 mAh g⁻¹ at a higher current density of 0.96 mA cm⁻². The rate capability of Ni-MOFs-based Li–O₂ batteries were further evaluated with a capacity cut-off of 600 mAh g⁻¹. The discharge plateau keeps nearly unchanged when the current densities increased from

0.12 to 0.96 mA cm⁻², even though a decrease is found at a current density of 0.96 mA cm⁻² (Fig. S3a). These results indicate that Ni-MOFs catalyst has high activity for ORR/OER and high rate capability.

The cycling stability of Ni-MOFs-based Li-O₂ batteries is assessed with different specific capacity limits. Fig. 3d and 3e present the voltage profiles and the variation of the discharge voltage terminal with a fixed capacity retention of 600 mAh g⁻¹, respectively. The battery ran 100 cycles with negligible voltage terminal drop (below 3%), which strongly guarantees high energy densities (energy density = voltage × capacity). More excitingly, a preliminary test showed that such batteries could stably operate for 170 cycles without obvious increased polarization (Fig. S3b). This indicates the high reversibility towards the formation and decomposition of the discharge products and rechargeability of Li-O₂ batteries. It is worth noting that such a long continuous operating time is rarely achieved by Li-O₂ batteries reported by far.^{34,35} We then increased the cut-off capacity and current density to larger values of 1080 mAh g⁻¹ and 0.72 mA cm⁻², respectively. To our surprise, the discharge voltage terminal still obtains 90% retention even after more than 80 cycles (Fig. 3f and 3g).

Fig. S4 shows six full discharge/charge cycles of the Ni-MOFs based batteries in a voltage range of 2.2–4.3 V at a current density of 0.36 mA cm⁻². The full discharge/charge capacities in the first three cycles are 6000/6492, 3700/3870, 3467/2473 mAh g⁻¹, respectively. The reversibility of Ni-MOFs based Li-O₂ batteries could be hampered by the possible electrolyte (TEGDME) and binder (PVdF) decomposition.^{36,37} To get into the reversible ORR/OER, cyclic voltammograms of Ni-MOFs-based batteries at a constant scan rate of 0.1 mV s⁻¹ are measured (Fig. S5a). The anodic and cathodic peaks only

slightly shift during the initial 3 cycles, further proving the high rechargeability. In comparison, the cycling performance of VC-72-based batteries is also tested (Fig. S5b). The discharge voltage terminal drops rapidly after only 28 cycles with a specific capacity limit of 500 mAh g⁻¹, excluding the possible performance contributions from catalytic activity of VC-72. In the other control experiments, Ni-MOFs-based batteries in Ar and Ni-foam-based batteries in O₂ showed extremely poor performance (Fig. S5c). Therefore, it can conclude that the electrochemical performance of Ni-MOFs-based batteries mainly stems from the O₂-involved reaction catalyzed by Ni-MOFs.

“Plastic Li-O₂ battery”

To confirm the practicability of Ni-MOFs-based cathode, we designed and assembled a plastic Li-O₂ battery (PLOB, Fig. 4a). Briefly, the PLOB consists of a lithium foil anode, a glass fiber separator, a cathode (Ni-MOFs coating on one piece of carbon paper), one plastic bag (cell case) and two electrode wires (Fig. 4b). The plastic bag close to the cathode side is dug many holes for O₂ transfer (Fig. 4c). The discharge/charge profiles are displayed in Fig. 4d. In the 1st cycle, it could provide an initial capacity of 4650 mAh g⁻¹ with a middle discharge voltage of 2.6 V, corresponding to an energy density of □537 (4650×16×2.6/360) Wh kg⁻¹ or 478 Wh kg⁻¹ (including consumed O₂ mass). This is much higher than that of commercial Li-ion batteries (130-180 Wh kg⁻¹). In the 7th cycle, the POLB showed a discharge capacity of 2150 mAh g⁻¹ with a middle discharge voltage of 2.5 V, corresponding to 239 Wh kg⁻¹ or 213 Wh kg⁻¹ (including consumed O₂ mass). It is worth noting that the preparation process of the PLOB is still in further optimization.

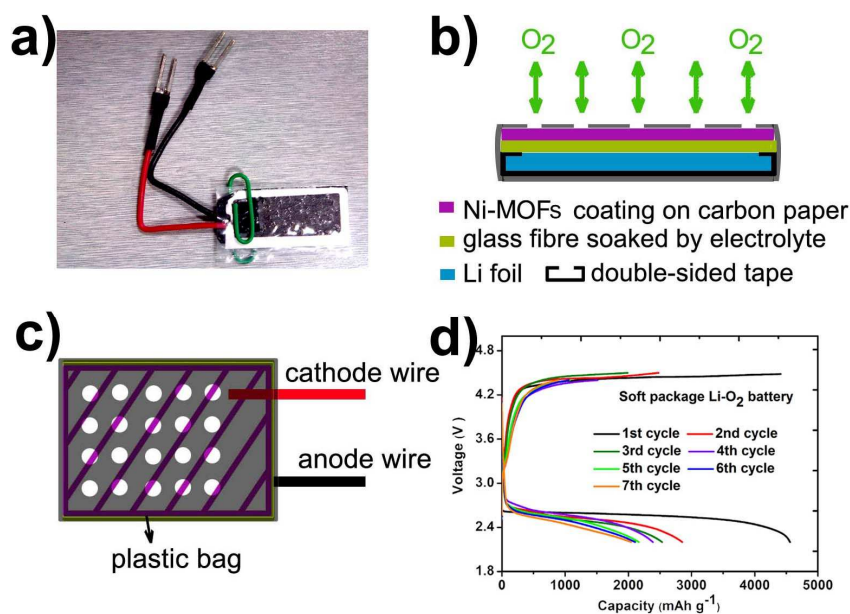


Fig. 4 Plastic Li-O₂ batteries assembled with Ni-MOFs and electrochemical performance. (a) A photograph of a plastic Li-O₂ battery. (b) Cross-sectional view and (c) top view of the scheme of the plastic Li-O₂ battery (soft package style). This consists of Li anode, separator soaked by electrolyte, cathode coated by Ni-MOFs/C, and plastic case with holes for oxygen entering. (d) Variation of voltage on the capacity. The capacity is based on the mass of Ni-MOFs/C (~16 mg) on cathode.

Reversibility of discharge products.

To further understand the electrochemical mechanism, Ni-MOFs-based electrodes for Li-O₂ batteries at different discharge/charge states were characterized. Six points were selected in the discharge/charge curves for detail tests (XRD, EIS, and SEM) (Fig. 5a). The XRD measurements were carried out (Fig. 5b). Clearly, the characteristic peaks of Ni-MOFs kept unchanged after the 1st discharge, indicating its stability under discharge. However, the XRD patterns also witnessed some changes. For the discharged cathode, in addition to the diffraction peaks of Ni-MOFs, C and Ni foam, the XRD patterns only indicate the formation of Li₂O₂ without other discharge by-products (such as LiOH). Additionally, the peaks of Li₂O₂ disappeared after recharge, suggesting that the products could fully decompose during the charge process. Raman spectrum further characterized the cathode after 50 cycles (Fig. S6). We can clearly observe Raman peaks indexed to Li₂O₂ with by-products Li₂CO₃ at the end of the 50th discharge, which probably came from the decomposition of electrolyte and binder. However, after the 50th recharge, the peaks of Li₂O₂ still disappeared, indicating that the rechargeability of Ni-MOFs based Li-O₂ batteries is maintained. This is crucial to the performance improvement of Li-O₂ batteries³⁸⁻⁴⁰. We also tested the electrochemical impedance spectroscopy (EIS) of Ni-MOFs-based batteries at different

states. The impedance in Fig. 5c shows that both interfacial resistance and charge-transfer resistance increase on discharging and almost recover to the initial state after recharging. The morphology evolution of the cathode has been investigated using SEM analysis. Compared with the pristine cathode (point I, Fig. 5d), the morphology of discharged cathode (point II, Fig. 5e) is similar to the pristine state, indicating that the Li₂O₂ was firstly formed inside of the nanopores of Ni-MOFs in the initial period of discharge. After that, large amount of Li₂O₂ were gradually deposited on the outside surface of Ni-MOFs (point III, Fig. 5f) and finally in the form of nanofibers after deep discharge (point IV, Fig. 5g). Theoretical calculations have concluded that Li₂O₂ surface is half metallic, while the bulk of Li₂O₂ is nonconductive.⁴¹ Therefore, the nanosized discharge products could provide more sufficient Li₂O₂-electrolyte interfaces and thus facilitate the decomposition of Li₂O₂ on charging. As expected, the nanofibrous morphology of Li₂O₂ disappeared first (point V, Fig. 5h). Afterwards, the recharged cathode was finally recovered to the pristine state (point VI, Fig. 5i). This accords well with the results of XRD and EIS analyses. These results indicate that Ni-MOFs-based cathode in Li-O₂ batteries can effectively accelerate the ORR process to form nanofiber like Li₂O₂ and facilitate the OER process to completely decompose this discharge product so as to guarantee the reduced overpotential and enhanced cycling stability.

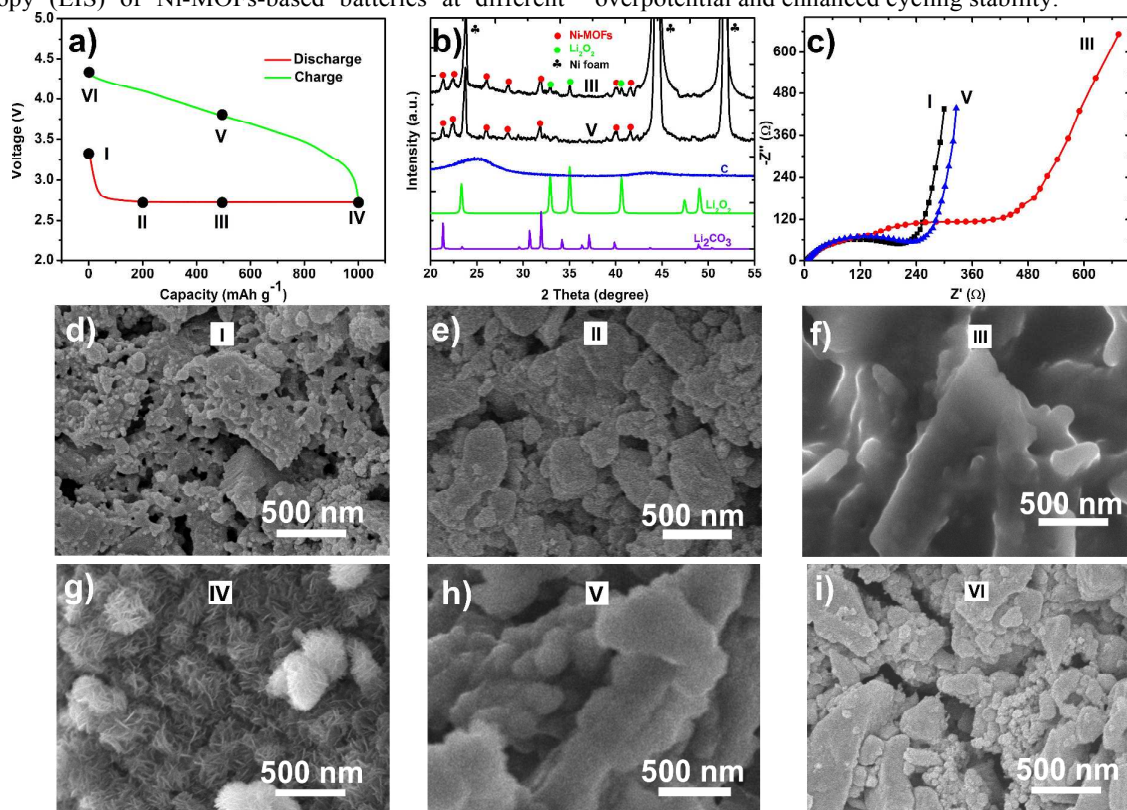
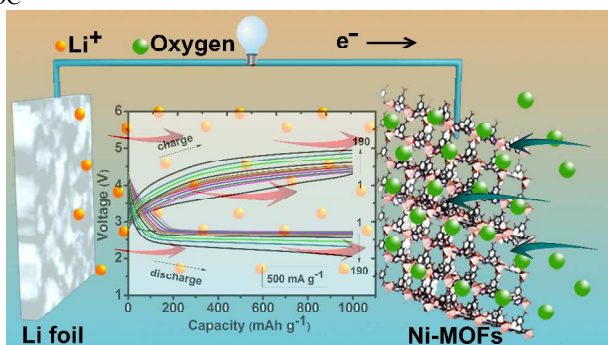


Fig. 5 Cathode rechargeability of the proposed Li-O₂ battery. (a) Discharge and charge curves with 6 points for process tests (XRD, EIS, and SEM). The 6 points correspond to six different states: I, before discharge; II, discharge to 200 mAh g⁻¹; III, discharge to 500 mAh g⁻¹; IV, discharge to 1000 mAh g⁻¹; V, recharge to 500 mAh g⁻¹; VI, recharge to 1000 mAh g⁻¹. (b) XRD patterns of and (c) EIS spectra of Ni-MOFs-based cathode at different discharge/charge state. SEM images of Ni-MOFs-based cathode (d) point I, (e) point II, (f) point III, (g) point IV, (h) point V, and (i) point VI. The current density is 500 mA g⁻¹.

- 1 Conclusion** 50
- 2 We have demonstrated that the operation of rechargeable Li-O₂ 51
 3 batteries with superior rechargeability, long cycling life, and 52
 4 high rate capability can be attainable by using the cathode 53
 5 catalyst of Ni-MOFs. This is owing to that Ni-MOFs possess 54
 6 open catalytic sites, large specific surface area, and especially 55
 7 uniform micro-nanostructures, all of which are beneficial for 56
 8 effective contact (electrolyte/catalytic metal sites) and mass 57
 9 transfer (O₂ & Li⁺). Such Ni-MOFs-based Li-O₂ batteries 58
 10 attained an enormous capacity of 9000 mAh g⁻¹ at 0.12 mA cm⁻² 59
 11 ². Remarkably, such batteries also exhibited a high round-trip 60
 12 efficiency of 80% with capacity limit of 600 mAh g⁻¹ at 0.6 mA 61
 13 cm⁻², and the voltage terminal can be stable for a preliminary 62
 14 test of 170 cycles. Moreover, we have used Ni-MOFs as the 63
 15 cathode catalyst to assemble “plastic rechargeable Li-O₂ 64
 16 batteries”, showing an energy density of ~478 Wh kg⁻¹ in the 65
 17 initial discharge. These results show that Ni-MOFs are 66
 18 promising materials as the cathode catalysts for rechargeable 67
 19 Li-O₂ batteries with high performance. 68
- 20 Acknowledgements** 70
- 21 This work was supported by National Programs of 973 (2011CB935900) 71
 22 NSFC (21231005 and 21322101), and MOE (B12015 and IRT13R30). We 72
 23 also thank Professor Jianrong Li at Beijing University of Technology for 73
 24 discussion on the structure of NiOFs. 74
- 25 Notes and references** 76
- 26 ¹Key Laboratory of Advanced Energy Materials Chemistry (Ministry 77
 27 Education), ²Collaborative Innovation Center of Chemical Science and 78
 28 Engineering, Nankai University, Tianjin, 300071, People’s Republic 79
 29 China. Tel/Fax: +86-22-23506808; E-mail: chenabc@nankai.edu.cn 80
 30 †Electronic Supplementary Information (ESI) available: XRD, BEIS 81
 31 additional electrochemical characterization. DOI:10.1039/b000000x/ 82
- 32 References:** 83
- 33 1. O. M. Yaghi, M. O’Keeffe, N. W. Ockwig, H. K. Chae, M. Eddaoudi, 84
 34 and J. Kim, *Nature*, 2003, **423**, 705–714. 85
 35 2. G. Férey, C. Serre, T. Devic, G. Maurin, H. Jobic, P. L. Llewellyn, G. 86
 36 D. Weireld, A. Vimont, M. Daturi and J. S. Chang, *Chem. Soc. Rev.*, 87
 37 2011, **40**, 550–562. 88
 38 3. J. P. Zhang, Y. B. Zhang, J. B. Lin and X. M. Chen, *Chem. Rev.*, 89
 39 2012, **112**, 1001–1033. 90
 40 4. T. D. Bennett and A. K. Cheetham, *Acc. Chem. Res.*, 2014, **47**, 91
 41 1555–1562. 92
 42 5. J. W. Liu, L. F. Chen, H. Cui, J. Y. Zhang, L. Zhang and C. Y. Su, 93
 43 *Chem. Soc. Rev.*, 2014, **43**, 6011–6061. 94
 44 6. Z. J. Zhang and M. J. Zaworotko, *Chem. Soc. Rev.*, 2014, **43**, 5444– 95
 45 5455. 96
 46 7. E. D. Bloch, W. L. Queen, R. Krishna, J. M. Zadrozny, C. M. Brown 97
 47 and J. R. Long, *Science*, 2012, **335**, 1606–1610. 98
 48 8. J. Canivet, A. Fateeva, Y. M. Guo, B. Coasne, D. Farrusseng, *Chem. 99
 49 Soc. Rev.*, 2014, **43**, 5594–5617. 100
9. L. Sarkisov, R. L. Martin, M. Haranczyk and B. Smit, *J. Am. Chem. 101
 Soc.*, 2014, **136**, 2228–2231. 102
10. F. Y. Cheng, J. Liang, Z. L. Tao and J. Chen, *Adv. Mater.*, 2011, **23**, 103
 1695–1715. 104
11. L. M. Zhou, T. R. Zhang, Z. L. Tao and J. Chen, *Nano Res.*, 2014, **7**,
 774–781.
12. M. Armand and J. M. Tarascon, *Nature*, 2008, **451**, 652–657.
13. F. Y. Cheng, J. Shen, B. Peng, Y. D. Pan, Z. L. Tao and J. Chen, *Nat. Chem.*, 2011, **3**, 79–84.
14. T. R. Zhang, Z. L. Tao and J. Chen, *Mater. Horiz.*, 2014, **1**, 196–206.
15. K. Zhang, X. P. Han, Z. Hu, X. L. Zhang, Z. L. Tao and J. Chen, *Chem, Soc. Rev.*, 2015, **44**, 699–728.
16. F. Y. Cheng and J. Chen, *Chem. Soc. Rev.*, 2012, **41**, 2172–2192.
17. Y. C. Lu, B. M. Gallant, D. G. Kwabi, J. R. Harding, R. R. Mitchell, M. S. Whittingham and Y. Shao-Horn, *Energy Environ. Sci.*, 2013, **6**, 750–768.
18. F. Y. Cheng and J. Chen, *Nat. Chem.*, 2012, **4**, 962–963.
19. Y. H. Kim, X. Lepró, R. Ovalle-Robles, R. H. B. and K. Kang, *Energy Environ. Sci.*, 2013, **6**, 3570–3575.
20. F. Y. Cheng and J. Chen, *Acta Chim. Sinica*, 2013, **71**, 473–477.
21. Z. Q. Peng, S. A. Freunberger, Y. H. Chen and P. G. Bruce, *Science*, 2012, **337**, 563–566.
22. D. F. Wu, Z. Y. Guo, X. B. Yin, Q. Q. Pang, B. B. Tu, L. J. Zhang, Y. G. Wang and Q. W. Li, *Adv. Mater.*, 2014, **26**, 3258–3262.
23. C. Y. Gao, S. X. Liu, L. H. Xie, Y. H. Ren, J. F. Cao and C. Y. Sun, *CrystEngComm*, 2007, **9**, 545–547.
24. Y. L. Zhao, L. Xu, L. Q. Mai, C. H. Han, Q. Y. An, X. Xu, X. Liu and Q. J. Zhang, *Proc. Natl. Acad. Sci. USA*, 2012, **109**, 19569–19574.
25. M. Kruk and M. Jaroniec, *Chem. Mater.*, 2001, **13**, 3169–3183.
26. M. R. Gao, W. C. Sheng, Z. B. Zhuang, Q. R. Fang, S. Gu, J. Jiang and Y. S. Yan, *J. Am. Chem. Soc.*, 2014, **136**, 7077–7084.
27. J. J. Xu, D. Xu, Z. L. Wang, H. G. Wang, L. L. Zhang and X. B. Zhang, *Angew. Chem. Int. Ed.*, 2013, **52**, 3887–3890.
28. B. D. McCloskey, D. S. Bethune, R. M. Shelby, T. Mori, R. Scheffler, A. Speidel, M. Sherwood and A. C. Luntz, *J. Phys. Chem. Lett.*, 2012, **3**, 3043–3047.
29. J. B. Park, J. Hassoun, H. G. Jung, H. S. Kim, C. S. Yoon, I. H. Oh, B. Scrosati and Y. K. Sun, *Nano Lett.*, 2013, **13**, 2971–2975.
30. R. Choi, J. Jung, G. Kim, K. Song, Y. I. Kim, S. C. Jung, Y. K. Han, H. Song and Y. M. Kang, *Energy Environ. Sci.*, 2014, **7**, 1362–1368.
31. G. Wu, N. H. Mack, W. Gao, S. G. Ma, R. Q. Zhong, J. T. Han, J. K. Baldwin and P. Zelenay, *ACS Nano*, 2012, **6**, 9764–9776.
32. T. Zhang and H. S. Zhou, *Nat. Commun.*, 2013, **4**, 1817–1823.
33. H. D. Lim, H. Song, J. Kim, H. Gwon, Y. Bae, K. Y. Park, J. Hong, H. Kim, T. Kim, Y. H. Kim, X. Lepró, R. O. Robles, R. H. Baughman and K. Kang, *Angew. Chem. Int. Ed.*, 2014, **126**, 1–7.
34. Z. K. Luo, C. S. Liang, F. Xu, Y. H. W, J. Chen, D. Liu, H. Y. Sun, H. Yang and X. P. Fan, *Adv. Funct. Mater.*, 2014, **24**, 2101–2105.
35. Y. G. Wang and Y. Y. Xia, *Nat. Chem.*, 2013, **5**, 445–447.
36. K. R. Ryan, L. Trahey, B. J. Ingram and A. K. Burrell, *J. Phys. Chem. C* 2012, **116**, 19724.
37. B. D. McCloskey, A. Speidel, R. Scheffler, D. C. Miller, V. Viswanathan, J. S. Hummelshøj, J. K. Nørskov and A. C. Luntz, *J. Phys. Chem. Lett.* 2012, **3**, 997.

- 1 38. X. P. Han, Y. X. Hu, J. G. Yang, F. Y. Cheng and J. Chen, *Chem.*
2 *Commun.*, 2014, **50**, 1497–1499.
3 39. X. P. Han, F. Y. Cheng, C. C. Chen, Y. X. Hu and J. Chen, *Nano*
4 *Res.*, 2015, **8**, 156–164.
5 40. X. F. Hu, X. P. Han, Y. X. Hu, F. Y. Cheng and J. Chen, *Nanoscale*,
6 2014, **6**, 3522–3525.
7 41. M. D. Radin, J. F. Rodriguez, F. Tian and D. J. Siegel, *J. Am. Chem.*
8 *Soc.*, 2012, **134**, 1093–1103.

9
10
11
12 TOC



13
14
15 The operation of rechargeable Li-O₂ batteries with long cycling life, high
16 rate capability, and large capacity can be attainable at room temperature
17 by using one cathode catalyst of Ni-MOFs, which possesses open metal
18 sites, large specific surface area, and especially uniform 3D micro-nano
19 structures.

20
21